Small- and wide-angle x-ray scattering studies of liquid–liquid phase separation in silicate melts

Chris J. Benmore, Oliver L G Alderman, Sophie R Benmore, Stephen K Wilke, and Richard J. K. Weber

Published version information

Citation: CJ Benmore et al. 'Small and wide angle x-ray scattering studies of liquid-liquid phase separation in silicate melts.' ACS Earth and Space Chemistry, vol. 4, no. 10 (2020): 1888-1894.

DOI: 10.1021/acsearthspacechem.0c00170

Article

Small and wide angle x-ray scattering studies of liquid-liquid phase separation in silicate melts

Chris J. Benmore, Oliver L G Alderman, Sophie R Benmore, Stephen K Wilke, and Richard J. K. Weber

ACS Earth Space Chem., **Just Accepted Manuscript** • DOI: 10.1021/acsearthspacechem.0c00170 • Publication Date (Web): 04 Sep 2020

Just Accepted

is published by the American Chemical Society. 1155 Sixteenth Street N.W., Washington, DC 20036

Small and wide angle x-ray scattering studies of liquid-liquid phase separation in silicate melts.

Chris J. Benmore[1], Oliver L.G. Alderman[2,3],
Sophie R. Benmore[2], Stephen K. Wilke[2], and Richard J.K. Weber[1,2]

[1] X-Ray Science Division, Advanced Photon Source,
Argonne National Laboratory, Argonne, IL 60439, USA
[2] Materials Development, Inc., Arlington Heights, IL 60004, USA
[3] ISIS facility, Rutherford Appleton Laboratory, Chilton, Oxfordshire, UK.

Abstract

Incongruent liquid-liquid phase separation is a common phenomenon in molten oxides, but there are few structural studies due to the high temperatures involved ca. >1600°C. Here we present a high-energy x-ray combined small/wide angle scattering (SAXS/WAXS) method that can directly probe non-equilibrium phase diagrams. The Porod exponent in the SAXS signal is extracted, which measures the roughness of the interface formed between different phases. Problematic volatilization of silica in Al_2O_3-, CaO-, and MgO-bearing silica-rich liquids were minimized using levitation, laser heating and rapid time-resolved measurements (lasting tens of seconds), to probe the kinetics of the phase separation process. The WAXS measurement simultaneously probes the local atomic structure of the liquid state and shows that the primary structural changes are associated with the SiO_2 network. Cation coordination numbers extracted from pair distribution functions support the model that the origin of phase separation in binary silicate systems is due to Coulombic repulsions between poorly screened cations. For CaO-SiO_2, the liquid-liquid phase separation is found to correlate with a pause in the temperature dependent atomic disorder associated with SiO_4 tetrahedra.

Keywords: silicate liquids, liquid-liquid, phase separation, x-ray diffraction, pair distribution function, aerodynamic levitation.

Introduction

Calcium-Magnesium-Aluminum-Silicate (CMAS) liquids formed in the early stages of the Earth and Moon, and their structure-related properties strongly influenced the evolution of these planetary bodies[1]. Binaries from the CMAS model system contain major crystal and mantle minerals, e.g. quartz, forsterite, anorthite, pyroxenes, garnets, spinels, perovskite and post-perovskite structures[2]. These silicate-rich liquids exhibit high viscosities, as indicated by their high-temperature viscous flow activation energies as a function of metal oxide composition[3]. Moreover, many silicate-rich melts have a tendency to phase separate upon cooling, and this has become an important phenomena in the development of metallurgical processing and glass-ceramics[4]. Many binary silicate melts display stable two-liquid immiscibility during cooling, and the widths of their immiscibility gaps have been shown to vary according to ionic potential (or field strength) and coordination number[5,6]. Moreover, the origin of phase separation in binary silicate systems has been attributed to Coulombic repulsions between poorly screened cations, bounded by bridging oxygen that are strongly polarized towards the silicon[7]. The chemically inhomogeneous liquids often form two-phase glasses, but little is known about their structural evolution, domain sizes, and the interface between the phases, all of which can effect rheological behavior.

Previous small angle scattering methods on fast quenched Al_2O_3-SiO_2 glasses have underestimated the consulate temperature by 575°C[8,9], which underscores the need for *in situ* measurements on the liquid state. Here we present a method that can potentially be used to probe immiscibility domes in binary silicate phase diagrams, while simultaneously providing information on average coordination numbers at high temperatures, which are not always possible using spectroscopic techniques[7]. We have performed temperature dependent small angle and wide angle x-ray scattering measurements (SAXS/WAXS) to investigate liquid-liquid (L-L) immiscibility in the Al_2O_3-SiO_2, CaO-SiO_2, and MgO-SiO_2 systems using aerodynamic levitation and laser heating. It is well known that incongruent volatilization of silica occurs at high-temperatures such that rapid measurements are required to minimize mass loss[10]. Furthermore, variable cooling rates and isothermal hold

times are required to probe the kinetics of the phase separation process. The advantages of simultaneous small-angle and wide-angle diffraction are widely recognized[11,12]. Our approach provides continuous coverage of reciprocal space by ensuring overlap between SAXS and WAXS patterns, and further extends the WAXS signal to high-Q by use of high-energy x-rays. In real space, the pair distribution function is obtained through a direct sine Fourier transform of the x-ray structure factor, S(Q), giving insight into the local structural arrangements[13].

Figure 1 shows that L-L immiscibility in CaO-SiO_2[14,15] and MgO-SiO_2[16,17] occurs in stable regions of their phase diagrams[18]. However, Al_2O_3-SiO_2[19–21] exhibits metastable immiscibility in the supercooled liquid region and spinodal behavior within the immiscibility dome. In our experiments, homogeneous melts of $30Al_2O_3$:$70SiO_2$ (AS30), $20CaO$:$80SiO_2$ (CS20), and $37.5MgO$:$62.5SiO_2$ (MS37.5) were obtained at high-temperatures, and the calcium and magnesium silicate liquids were also measured as a function of controlled cooling. All compositions were found to form phase-separated glasses after cooling to room temperature.

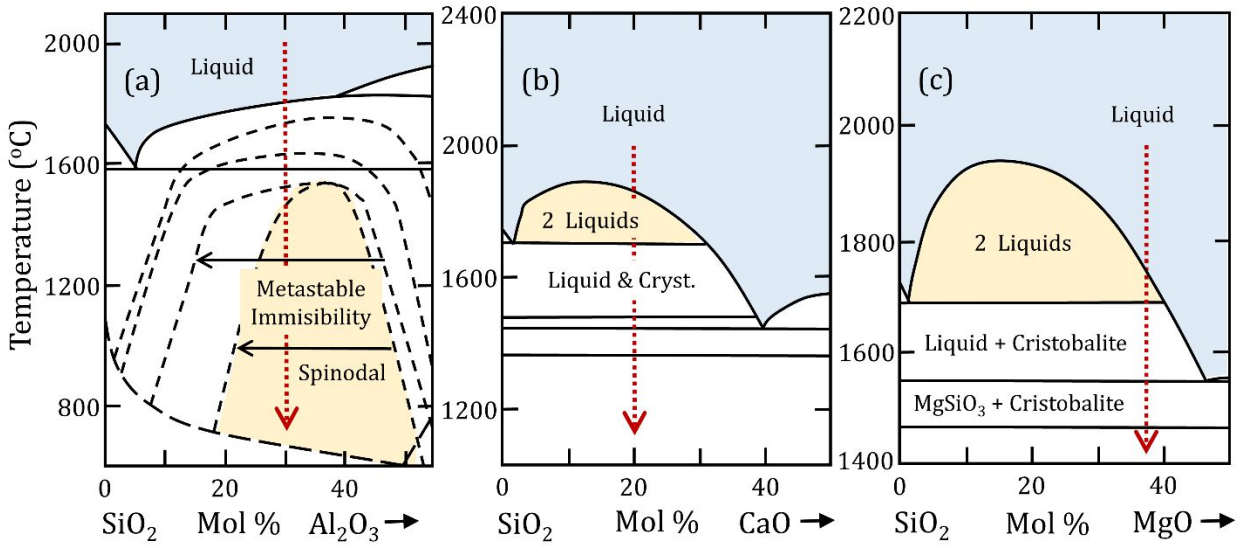

Figure 1. Phase diagrams of (a) Al_2O_3-SiO_2[4] (b) CaO-SiO_2[8,9] and (c) MgO-SiO_2[10,11]. The dashed black lines represent metastable phase boundaries and the red dotted lines represent the compositions studied here.

Methods

High energy x-ray diffraction measurements were performed on beamline 6-ID-D at the Advanced Photon Source using an incident energy of 80keV. Simultaneous SAXS and WAXS detector measurements were carried out using a dual detector system with a continuous Q coverage over the range ~0.03 to ~19 Å^{-1}, including an overlap region of ΔQ ~1.5 Å^{-1}. Dexela 2315-MAM detectors (active area 230 mm × 145 mm and square 74.8 μm pixels) were mounted in each of the SAXS and WAXS positions at sample to detector distances of ~230cm and ~28cm respectively. Careful alignment of the optics ensured slit scattering was not present in the diffusely scattered intensity. A tube with Kapton windows was positioned between the SAXS and WAXS detectors, and evacuated to reduce background air scatter in the SAXS detector. A chamfered beamstop was positioned against the downstream window[13].

The WAXS detector diffraction patterns were calibrated using NIST standard CeO_2, and the SAXS detector was calibrated using silver behenate to determine the precise sample to detector distances and tilts. The SAXS and WAXS data sets were analyzed using the *Fit2D* software[22] and corrected for flat field, polarization, rotation and tilt. The program *PDFgetX2*[23] was used to correct for background, oblique incidence, absorption and detector efficiency effects. Applying the correct transmission factor prior to subtracting the background was essential to obtain good agreement between SAXS and WAXS in the overlap region, where signal-to-background ratio was at its lowest. *PDFgetX2* was used to normalize the WAXS, I(Q), data to the sample self-scattering in absolute electron units, and the background corrected SAXS intensity was normalized to the WAXS data in the Q-space overlap region. The SAXS and WAXS data were spliced together at Q~0.5 Å^{-1} to obtain the total x-ray structure factor, S(Q). S(Q) was truncated at a maximum Q-value, Q_{max}, corresponding to a node at Q~ 18 Å^{-1} and Fourier transformed using a Lorch modification function to ensure reasonable r-space resolution and minimize spurious ripples to yield the total pair distribution function: T(r).

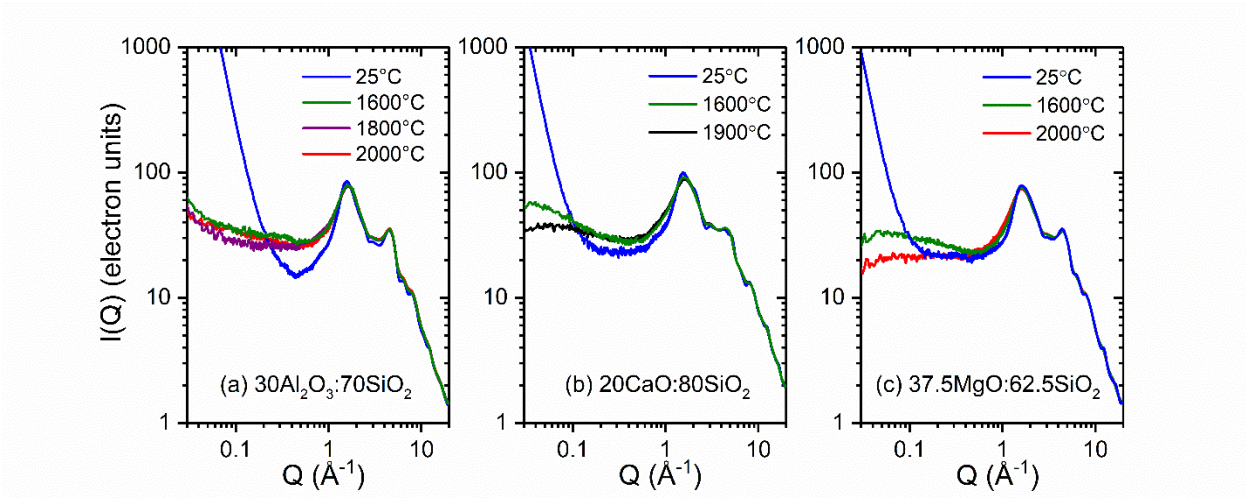

Figure 2. Normalized SAXS-WAXS intensities obtained from isothermal measurements on single phase liquid and two phase glassy silicates.

Details of the aerodynamic levitation and laser system have previously been described in depth in other publications[24,25]. Here, 2-3mm diameter spheres of 30:70 mole % Al_2O_3:SiO_2, 20:80 mole % CaO:SiO_2, and 37.5:62.5 mole % MgO:SiO_2 were prepared with masses ranging from 18-35mg. The spheres were levitated on an oxygen gas jet and melted from above using a 400W CO_2 laser. The typical mass loss during the experiments was ~1% indicating, at most, only a small composition change. Two types of x-ray diffraction experiments were conducted: (i) isothermal experiments, maintaining a fixed temperature for 50s, and (ii) quenching experiments using 4s detector exposures during different quench rates. For the AS30 sample, fast quench rates (~100°C/s) were required to obtain a glass, so only isothermal experiments were feasible in order to obtain adequate statistics in the WAXS signal. For the CS20 sample a quench rate of 25°C/s was required to form a glass, but for MS37.5 a rate of 5°C/s was sufficient.

Results

The SAXS/WAXS data for all three samples shown in Figure 2 show a dramatic rise in the SAXS (Porod) region in the room temperature glassy phase compared to the corresponding high temperature melts. However, the changes in the WAXS region are much more subtle and generally show a slight sharpening of the peaks at lower temperatures. The

growth of the SAXS intensity upon quenching for CS20 and MS37.5 starts around the temperature of the liquid+crystal/crystal boundary of the stable phase diagrams (figure 1), see figure 3.

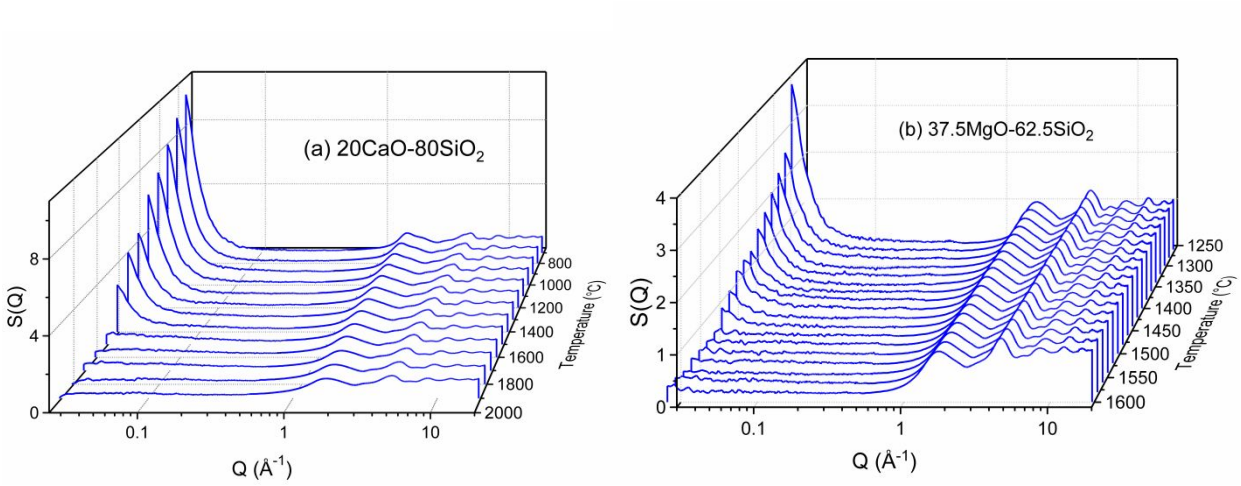

Figure 3. The SAXS-WAXS total x-ray structure factor changing from liquid to glass as a function of temperature during the quenching experiments for CS20 and MS37.5.

The changes in short range order in real space and the corresponding total pair distribution functions for the isothermal experiments are shown in Figure 4. Coordination numbers were extracted using NXfit[26] on the 2-phase glasses using estimated number densities of 0.074 atoms Å^{-3} for AS30[3] and CS20[27,28], and 0.082 atoms Å^{-3} for MS37.5[29]. The Si-O bond length at a distance of $r_{Si\text{-}O}$=1.62-1.68 Å was fixed to correspond to regular tetrahedral i.e. N_{SiO}=4, and the O-O distance kept at $r_{O\text{-}O}=\sqrt{(8/3)}r_{Si\text{-}O}$~2.6 Å with $N_{OO}=12(c_{Si}/c_O)$[30]. The metal-oxygen peaks are broader than the Si-O, reflecting a distribution of distorted metal-oxygen MO_n polyhedra. The effective crystallographic ionic radii given by Shannon and Prewitt[31] indicate $r_{Si\text{-}O}$~ 1.64 Å for SiO_4, $r_{Al\text{-}O}$=1.77 Å for AlO_4, 1.87 Å for AlO_5 and 1.935 Å for AlO_6. For AS30, there are a broad distribution of Al-O correlations that overlap with the Si-O peak, and a three Gaussian fit at these fixed bond distances yielded total $N_{Al\text{-}O}$ coordination numbers of 4.4±0.3 (liquid) and 4.5±0.3 (glass), indicating a significant fraction of the polyhedra can be attributed to AlO_4. A similar analysis on MS37.5 found longer Mg-O bonds at ~2.3 Å were required to provide a good fit, in addition to Gaussians at $R_{Mg\text{-}O}$=1.95 Å for MgO_4, 2.05 Å for MgO_5 and 2.125 Å for MgO_6, presumably due to the heavily distorted polyhedra. These fits gave average Mg-O coordination numbers of

$N_{Mg\text{-}O=}$5.1±0.3 (liquid) and 4.8±0.3 (glass). The Ca-O peak is known to exhibit a distribution of both long and short bonds in the melt[27], and to obtain a good fit short Ca-O bonds at ~2.1 Å were needed in addition to Gaussians at $R_{Ca\text{-}O}$=2.40Å for CaO_6 and 2.47 Å for CaO_7. The fits yielded average Ca-O coordination numbers of $N_{Ca\text{-}O=}$6.5±0.3 (liquid) and 6.6±0.3 (glass). More accurate values for the coordination numbers require computer modeling to account for all the overlapping correlations within the 3D structure. The variation in bond distances correlate with changes in the ion size[31], the metal-oxygen coordination fits were all found to be asymmetric, see figure 4.

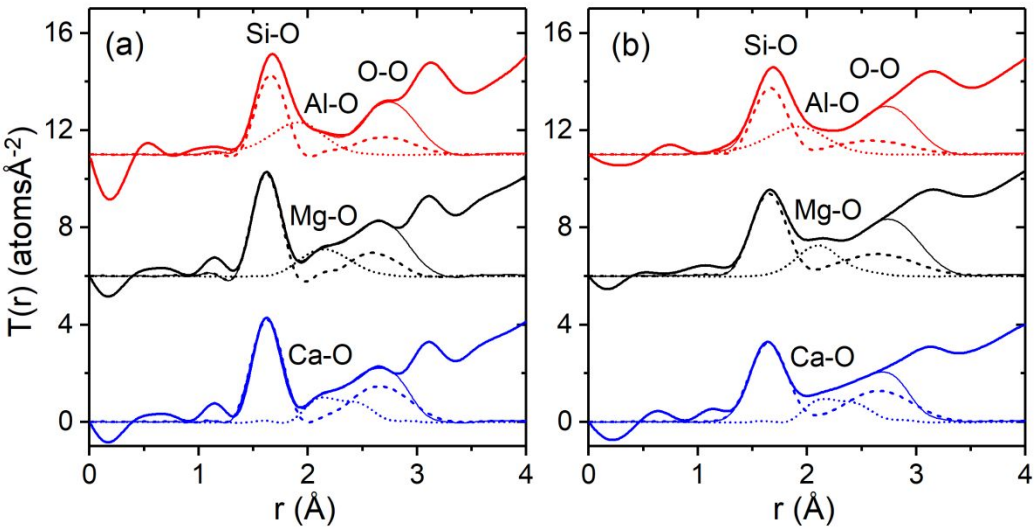

Figure 4. Total x-ray pair distribution functions for the isothermal experiments on binary silicates in the (a) room temperature glass and (b) liquid at 1600°C. The PDF data (thick solid lines) are shown as a function of increasing cation size: $30Al_2O_3$:$70SiO_2$ (top), 37.5MgO:62.5SiO_2 (middle) and 20CaO:80SiO_2 (bottom). The Gaussian fits described in the text correspond to the Si-O and O-O correlations associated with SiO4 tetrahedra (dashed line), the modifier cation-oxygen correlations (dotted line) and the total fit which includes short modifier O-O correlations (thin solid line).

Discussion.

Markhasev and Sedletskii[5] have argued that immiscibility fields expand with a decrease in ionic radius of the modifier, because it is harder for smaller modifier cations to find coordination environments within a highly polymerized flexible silica network. While some of the Si bonds to the cation-rich structure to satisfy the modifiers coordination requirements, the excess silica forms the second polymerized phase. An exhaustive review of 41 binary silicate systems by Hudon and Baker[7] identified three groups of cations that exhibit different immiscibility behaviors: (1) Those with a large ionic radius >87.2pm and coordination number ≥5, for which miscibility gap increases linearly with increasing ionic potential e.g. the CaO-SiO_2 system. (2) *Amphoteric* cations with small ionic radii <87.2pm (but >26pm corresponding to Si^{4+}) and at least two coordination number environments. One of which must be 4 and the other 5 or higher e.g. the Al_2O_3-SiO_2 and MgO-SiO_2 systems. (3) Cations with variable crystal field stabilization energies that are difficult to predict.

$30Al_2O_3$-$70SiO_2$.

The AS30 composition studied here lies midway between SiO_2 and mullite (which exhibits a range of compositions close to $3Al_2O_3.2SiO_2$) which congruently melts at 1850°C. Glass formation and stability decreases as the alumina content increases, and for >30 mol.% only very rapid quenching has been found to produce glasses[10], consistent with our findings. High silica content Al_2O_3-SiO_2 melts phase-separate readily upon cooling to form a uniform dispersion of amorphous microspheres within a silica-rich glassy matrix[10]. Thermal treatment leads to crystallization of dispersed mullite microspheres[32]. The two liquid phase separation occurs through the mechanism of nucleation and growth in the composition regions 7-20 mol% and 35-55 mol% alumina, and spinodal decomposition can occur in the unstable region in-between. This has been confirmed by the rapid quenching of glasses at ~30 mol% alumina, which produces an interconnected fine microstructure of irregularly shaped alumina-rich particles regularly distributed in a silica rich glass in approximately similar volumes[10].

Gibbs[33] described two distinct thermodynamic conditions for liquid-liquid immiscibility: (i) a spinodal region in which the host phase is unstable with respect to continuous separation, and (ii) a nucleation barrier outside this area, whereby once critical nuclei are formed they grow according to classical nucleation theory. Composition fluctuations grow in amplitude as phase boundaries are being established. It is the *roughness* of these composition gradients in this boundary region that is probed in the Porod regime of our measured SAXS signals. Porod's law states that if the interface between particles is flat, the scattering intensity reaches an asymptotic limit of $I(Q) \sim BQ^{-n}$ where the Porod exponent n=4 and *S* is the surface area of the particles. In this study, for AS30 the exponent was found to be $n \approx 1$ at 1600°C indicating some degree of density fluctuations in the liquid and n was about 4 at 25°C confirming a smooth interface between the two glassy phases.

Early structural interpretations of the Al_2O_3-SiO_2 system suggested aluminum ions replace silicon ions in tetrahedral coordination and form oxygen triclusters to maintain charge balance[34]. Recent high energy x-ray diffraction data show a strong distortion of the SiO_4 tetrahedral units in aluminosilicates with low Al_2O_3 content, and a breakdown of intermediate range order as alumina is added[3]. Diffraction and modeling studies on supercooled $CaSiO_3$, which show octahedral metal ion polyhedra tend to edge share with each other and polymerize upon cooling, while SiO_4 tetrahedra in liquid silica naturally corner share[35]. Our AS30 our results show overlapping Si-O and Al-O contributions, that only sharpens slightly upon quenching with $N_{AlO} \sim 5$, consistent with a distribution of distorted AlO_4, AlO_5, and AlO_6 polyhedra[3]. It has been argued that the presence of AlO_4 causes bonds to exhibit a covalent character with neighboring oxygens, making them strongly polarized towards the cation[7]. Our low Al-O coordination number is consistent with the presence of some AlO_4 polyhedra, that have bonds with a covalent component that can efficiently screen the nucleus. The screening associated with AlO_4 units in the melt considerably reduces the electrostatic repulsions with other cations reducing immiscibility and resulting in metastability.

$MgO-SiO_2$ and $CaO-SiO_2$ quenching studies.

The MS37.5 composition is on the edge of the 2-liquid region in the stable phase diagram. Here, our quenching experiments pass from the single to two liquid state at ~1730°C, into the liquid+cristobalite region between 1546-1687°C, and the $MgSiO_3$+cristobalite region between 1465-1546°C (Figure 1c). For liquid $MgSiO_3$, diffraction and modeling studies have found a mean MgO coordination number of 4.8 (integrating up to 2.8 Å)[20]. Our results on MS37.5 yield a higher value of N_{Mg-O}=5.2 consistent with the presence of distorted MgO_4, MgO_5, and MgO_6 polyhedra[36]. Consequently, as with Al_2O_3-SiO_2, $MgO-SiO_2$ falls into the amphoteric category. However, the slightly higher cation coordination number leads to stable phase separation.

In CS20, liquid-liquid phase separation is present between 1700-1855°C in the stable phase diagram, cristobalite+liquid forms between 1480-1700°C and tridymite+liquid between 1440-1480°C (Figure 1b). Liquid $CaSiO_3$ shows a substantial broadening of the first Ca–O bond length distribution in the pair distribution function of the melt compared to the glass[27]. This broadening has been explained by a redistribution of Ca–O bond lengths of primarily 6- and 7-fold coordinated Ca-polyhedra, toward longer distances in the liquid. As high temperature liquid $CaSiO_3$ is cooled, it has been demonstrated that dispersed short chains of edge-shared Ca octahedra polymerize within the silicate network[35]. Hess[6] has argued that when Ca^{2+} is added to liquid SiO_2, calcium cations that are partly or wholly coordinated by bridging oxygens are poorly shielded, because the oxygens have strong covalent bonds with Si^{4+}. As a consequence substantial Coulombic repulsions occur between network modifying cations, which leads to stable phase separation.

In order to correlate the rise in SAXS intensity associated with L-L phase separation we fit the log of the SAXS intensity (interface roughness) versus log temperature with a straight line to extract the Porod exponent: n. For both CS20 and MS37.5, within the 2 phase liquid region, $>T_{L-L}$, the Porod exponent tends to approximately zero, indicating no heterogeneity in the liquid up to a length-scale of ~200Å. The exponent n is found to decrease sharply upon cooling to a value of n~3 to 4 between T_{L-L} and T_{C-L}, as the interface

between the two phases becomes smoother. This is far below the L-L immiscibility dome indicating that our measurements were not in equilibrium. The flat boundaries appear to be established by the time the SiO_2 glass transition temperature, T_g^{SiO2}, is reached. Viscosity measurements on high temperature alkaline earth binary silicate liquids have been shown to exhibit Arrhenius behavior in the silica-rich region[37,38]. This behavior is expected for strong liquids with good glass forming ability. In this spirit, we find that the temperature dependence of the surface roughness between phases (Porod exponent) can be adequately described using an Arrhenius equation, as shown in figure 6. From this we determine that the phase separation on the few hundred Angstrom length-scale in CS20 occurs at 1556±50°C and in MS37.5 at 1527±10°C. Despite systematic errors in the data, due to the temperature gradient across the sample from top to bottom, differences in metal ion content and the variation in quenching rates, the change in n with temperature between the calcium- and magnesium-silicate liquids appears to be similar. This is consistent with the polymerization of the host silicate matrix upon cooling being a major factor during the phase separation process.

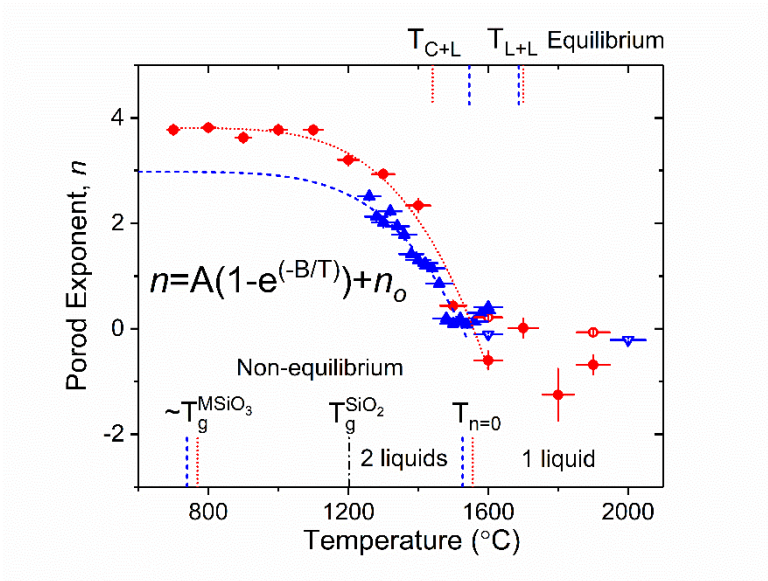

Figure 5. Temperature variation of the Porod exponent, n, in I(Q) for liquid 20CaO:80SiO_2 (red circles denotes quenched sample experiments and red open circles the isothermal measurements) and liquid 37.5MgO:62.5SiO_2 (blue solid up-triangles denotes quenched sample experiments and blue open-down triangles the isothermal measurements). The curves represent Arrhenius fits to the data. The markings at the top correspond to the

equilibrium phase diagram temperatures: the lower 2-phase liquid boundary (T_{L+L}) and the crystal plus liquid boundary below (T_{C+L}). The markings at the bottom correspond to the non-equilibrium temperatures: the pure SiO_2 glass transition temperature ($T_g^{SiO_2}$), the single phase $MSiO_3$ glass transition temperatures ($T_g^{MSiO_3}$) and the temperatures at which the fits cross n=0 ($T_{n=0}$).

Both quenching studies show a subtle (<1%) shortening of the average Si-O bond and lengthening of the O-O distance upon cooling from a liquid to a glass. The most notable effects in the x-ray pair distribution functions is the expected sharpening of all peaks with decreasing temperature, see Figure 4. Similar results have been reported by Benmore *et al.*[35] for $CaSiO_3$, upon quenching from a liquid to a glass; there it was argued that the presence of isosbestic points in the diffraction patterns was consistent with the polymerization of CaO_6 edge shared polyhedra. In this study the presence of isosbestic points are not apparent and the changes in the x-ray pair distribution function are dominated by changes in the silicate network rather than calcium polymerization i.e. the main local changes are associated with the Si-O bond intensity at ~1.64 Å and Si-Si distance at ~3.1 Å. The atomic disorder (root mean square deviation from the average atomic position) within the structure is directly related to the width of each individual atom pair correlation, so in Figure 5 we plot the full width half maximum (FWHM) of the Si-O bond length distribution in CS20 as a function of temperature. Time resolved studies on high temperature liquid silica by Skinner *et al.*[39] have shown a constant FWHM of the Si-O peak for temperatures above ~1227°C and a linear decrease in Si-O bond ordering as the temperature is decreased below that temperaure. For CS20, three regions can be identified corresponding to the changes in the Si-O FWHM peak:

(i) Normal behavior - a linear increase in Si-O bond ordering with decreasing temperature (i.e. thermal ordering) is initially observed in the homogenous stable liquid region.

(ii) a plateau in the atomic ordering within SiO_4 tetrahedra occurs as the 2-phase boundary regions are established. Although thermal ordering will continue to increase with decreasing temperature, phase separation will lead to the

formation of polymerized silica-rich regions with 4-bridging oxygens (Q^4 species) and silica-poor regions which have fewer bridging oxygens e.g. Q^2 species, leading to an overall Si-O peak broadening.

(iii) once $T_g^{SiO_2}$ is reached the phase boundaries have been established and the glassy silica-rich matrix becomes frozen in such that thermal ordering dominates again.

An identical analysis on MS73.5 was inconclusive due to larger error-bars associated with the FWHM and the narrower temperature range.

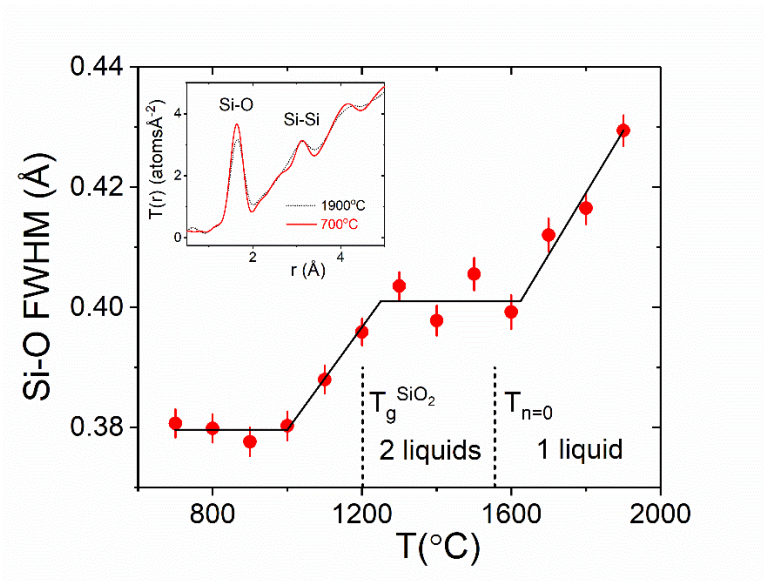

Figure 6. The change in full width half maximum of the Si-O peak upon cooling. Insert. The total pair distribution functions of $20CaO:80SiO_2$ liquid and glass. The SiO_2 glass transition temperature ($T_g^{SiO_2}$) and temperature at which phase separation begins in the SAXS signal ($T_{n=0}$) are marked. The line is a guide to the eye.

Conclusions

Understanding stable and metastable liquid-liquid immiscibility is important for predicting the properties of natural magmatism and melts. Although this is a common phenomenon of many binary silicate systems, it is difficult to determine the metal-oxygen coordination numbers in the molten state. The coordination numbers obtained here for

Al_2O_3-, CaO- and MgO-silicate melts are consistent with the model proposed by Hudon and Baker[7], that asserts the presence of 4-fold cations can efficiently polarize a neigbouring oxygen and exhibit strong covalent character. In their model, shared electrons that surround both the anion and cation shield the charge of the cation reducing the repulsions of the other modifier cations, narrowing the immiscibility gap or making it metastable in the case of Al_2O_3-SiO_2. However, more extensive studies are needed to map out the widths of the immiscibility gaps, to test if the model holds for these and other systems. In addition, the temperature of the upper consolute point (solvus) are still unkown in many silicate systems due to the high temperatures involved, and provides another avenue for future studies.

While the SAXS/WAXS/high-temperature instrumentation presented here is shown to be sensitive to nanoscale liquid-liquid phase separation, it does not appear that our measurements reached equilibrium because the SAXS signal is observed far below the equilibrium dome. This suggests that complex kinetics can play an important role in determining the morphology of the resulting materials e.g. in the macroscopic structural evolution of plantery materials such as chondrules that often form from supercooled drolets of molten oxides. In order to explore the equilibrium phase diagram, time resolved studies of longer durations are required, either isothermally or at slower cooling rates, although such experiments will limited by the evaporation of SiO_2.

Acknowledgements

Anthony Tamalonis (MDI) is thanked for help with design and integration of the two detector system and Doug Robinson (APS) for advice about x-ray detector selection and calibration. This research used resources of the Advanced Photon Source, a U.S. Department of Energy (DOE) Office of Science User Facility operated for the DOE Office of Science by Argonne National Laboratory under Contract No. DE-AC02-06CH11357. Work by MDI was supported under DOE contract number DE-SC0015241 and NASA grant number 80NSSC18K0059.

References.

(1) Poirier, J.-P. *Introduction to the Physics of the Earth's Interior*; Cambridge University Press, 2000. https://doi.org/10.1017/CBO9781139164467.

(2) Jahn, S.; Madden, P. A. Modeling Earth Materials from Crustal to Lower Mantle Conditions: A Transferable Set of Interaction Potentials for the CMAS System. *Phys. Earth Planet. Inter.* **2007**, *162* (1–2), 129–139. https://doi.org/10.1016/j.pepi.2007.04.002.

(3) Wilding, M. C.; Benmore, C. J.; Weber, J. K. R. High-Energy X-Ray Diffraction from Aluminosilicate Liquids. *J. Phys. Chem. B* **2010**, *114* (17), 5742–5746. https://doi.org/10.1021/jp907587e.

(4) Khater, G. A. Glass-Ceramics in the CaO-MgO-Al2O3-SiO2 System Based on Industrial Waste Materials. In *Journal of Non-Crystalline Solids*; North-Holland, 2010; Vol. 356, pp 3066–3070. https://doi.org/10.1016/j.jnoncrysol.2010.02.030.

(5) B. I. Markhasev, I. D. S. Certain regularities of structure in the melts of Me2O3–SiO2 systems http://www.mathnet.ru/php/archive.phtml?wshow=paper&jrnid=dan&paperid=29181&option_lang=eng (accessed Jun 29, 2020).

(6) Hess, P. C. Upper and Lower Critical Points: Thermodynamic Constraints on the Solution Properties of Silicate Melts. *Geochim. Cosmochim. Acta* **1996**, *60* (13), 2365–2377. https://doi.org/10.1016/0016-7037(96)00095-6.

(7) Hudon, P.; Baker, D. R. The Nature of Phase Separation in Binary Oxide Melts and Glasses. I. Silicate Systems. *J. Non. Cryst. Solids* **2002**, *303* (3), 299–345. https://doi.org/10.1016/S0022-3093(02)01043-8.

(8) Jantzen, C. M.; Schwahn, D.; Schelten, J.; Herman, H. The SiO2-Al2O3 System. I: Later Stage Spinodal Decomposition and Metastable Immiscibility. *Phys. Chem. Glas.* **1981**, *22*, 122–137.

(9) Aver'yanov, V.; Areshev, M.; Golubkov, V.; Stekla, L. D.-F. K.; 1984, U. Phase Separation in the Al2O3-SiO2 System. *Sov. J. Glas. Phys. Chem.* **1984**, *10*, 155–162.

(10) Macdowell, J. F.; Beall, G. H. Immiscibility and Crystallization in Al2O3-SiO2 Glasses. *J. Am. Ceram. Soc.* **1969**, *52* (1), 17–25. https://doi.org/10.1111/j.1151-2916.1969.tb12653.x.

(11) Glatter, O.; Kratky., O. *Small Angle X-ray Scattering.*; John Wiley & Sons, Ltd, 1982. https://doi.org/10.1002/actp.1985.010360520.

(12) Benmore, C. J. A Review of High-Energy X-Ray Diffraction from Glasses and Liquids. *ISRN Mater. Sci.* **2012**, *2012*, 1–19. https://doi.org/10.5402/2012/852905.

(13) Benmore, C. J.; Alderman, O. L. G.; Robinson, D.; Jennings, G.; Tamalonis, A.; Ilavsky, J.; Clark, E.; Soignard, E.; Yarger, J. L.; Weber, J. K. R. Extended Range X-Ray Pair Distribution Functions. *Nucl. Instruments Methods Phys. Res. Sect. A Accel. Spectrometers, Detect. Assoc. Equip.* **2020**, *955*, 163318-1–8. https://doi.org/10.1016/j.nima.2019.163318.

(14) DeCapitani, C.; Kirschen, M. A Generalized Multicomponent Excess Function with Application to Immiscible Liquids in the System CaO-SiO2-TiO2. *Geochim. Cosmochim. Acta* **1998**, *62* (23–24), 3753–3763. https://doi.org/10.1016/S0016-7037(98)00319-6.

(15) Kim, S. S.; Sanders, T. H. Thermodynamic Modeling of the Miscibility Gaps and the Metastable Liquidi in the MgO-SiO2, CaO-SiO2 , and SrO-SiO2 Systems. *J. Am. Ceram. Soc.* **1999**, *82* (7), 1901–1907. https://doi.org/10.1111/j.1151-2916.1999.tb02014.x.

(16) Wu, P.; Eriksson, G.; Pelton, A. D.; Blander, M. Prediction of the Thermodynamic Properties and Phase Diagrams of Silicate Systems-Evaluation of the FeO-MgO-SiO2 System. *ISIJ Int.* **1993**, *33* (1), 26–35. https://doi.org/10.2355/isijinternational.33.26.

(17) Hillert, M.; Wang, X. A Study of the Thermodynamic Properties of MgO-SiO2 System. *Calphad* **1989**, *13* (3), 253–266. https://doi.org/10.1016/0364-5916(89)90005-9.

(18) Ararnaki S. and Roy R. The Mullite-Corundum Boundary in the Systems MgO-Al2O-SiO2 and CaO-Al2O3-SiO2. *J. Am. Ceram. Soc.* **1959**, *42* (12), 644–645.

(19) Risbud S.H. and Pask J.A. Calculated Thermodynamic Data and Metastable Immiscibility in the System SiO2-Al2O3. *J. Am. Ceram. Soc.* **1977**, *60* (9–10), 418–424.

(20) Risbud S. and Pask J.A. On the Location of Metastable Immiscibility in the System SiO2-Al2O3. *J. Am. Ceram. Soc.* **1979**, *62*, 214–215.

(21) Aramaki S. and Roy R. Revised Phase Diagram for the System Al2O3-SiO2. *J. Am. Ceram. Soc.* **1962**, *45* (5), 229–242.

(22) Hammersley, A. P. FIT2D: A Multi-Purpose Data Reduction, Analysis and Visualization Program. *J. Appl. Crystallogr.* **2016**, *49*, 646–652. https://doi.org/10.1107/S1600576716000455.

(23) Qiu, X.; Thompson, J. W.; Billinge, S. J. L. PDFgetX2: A GUI-Driven Program to Obtain the Pair Distribution Function from X-Ray Powder Diffraction Data. *J. Appl. Crystallogr.* **2004**, *37* (4), 678–678. https://doi.org/10.1107/S0021889804011744.

(24) Weber, J. K. R.; Benmore, C. J.; Skinner, L. B.; Neuefeind, J.; Tumber, S. K.; Jennings, G.; Santodonato, L. J.; Jin, D.; Du, J.; Parise, J. B. Measurements of Liquid and Glass Structures Using Aerodynamic Levitation and In-Situ High Energy x-Ray and Neutron Scattering. *J. Non. Cryst. Solids* **2014**, *383*, 49–51. https://doi.org/10.1016/j.jnoncrysol.2013.03.035.

(25) Benmore, C. J.; Weber, J. K. R. Aerodynamic Levitation, Supercooled Liquids and Glass Formation. *Adv. Phys. X* **2017**, *2* (3), 717–736. https://doi.org/10.1080/23746149.2017.1357498.

(26) Pickup, D.; Moss, R.; Newport, R. *NXFit* : A Program for Simultaneously Fitting X-Ray and Neutron Diffraction Pair-Distribution Functions to Provide Optimized Structural Parameters. *J. Appl. Crystallogr.* **2014**, *47* (5), 1790–1796. https://doi.org/10.1107/S160057671401824X.

(27) Skinner, L. B.; Benmore, C. J.; Weber, J. K. R.; Tumber, S.; Lazareva, L.; Neuefeind, J.; Santodonato, L.; Du, J.; Parise, J. B. Structure of Molten CaSiO3: Neutron Diffraction Isotope Substitution with Aerodynamic Levitation and Molecular Dynamics Study. *J. Phys. Chem. B* **2012**, *116* (45), 13439–13447. https://doi.org/10.1021/jp3066019.

(28) Micoulaut, M.; Malki, M.; Simon, P.; Canizares, A. On the Rigid to Floppy Transitions in Calcium Silicate Glasses from Raman Scattering and Cluster Constraint Analysis. *Philos. Mag.* **2005**, *85* (28), 3357–3378. https://doi.org/10.1080/14786430500157029.

(29) Kohara, S.; Akola, J.; Morita, H.; Suzuya, K.; Weber, J. K. R.; Wilding, M. C.; Benmore, C. J. Relationship between Topological Order and Glass Forming Ability in Densely Packed Enstatite and Forsterite Composition Glasses. *Proc. Natl. Acad. Sci. U. S. A.* **2011**, *108* (36), 14780–14785. https://doi.org/10.1073/pnas.1104692108.

(30) Alderman, O. L. G.; Hannon, A. C.; Holland, D.; Feller, S.; Lehr, G.; Vitale, A. J.; Hoppe, U.;

Zimmerman, M. V.; Watenphul, A. Lone-Pair Distribution and Plumbite Network Formation in High Lead Silicate Glass, 80PbO·20SiO2. *Phys. Chem. Chem. Phys.* **2013**, *15* (22), 8506–8519. https://doi.org/10.1039/c3cp51348c.

(31) Shannon, R. D.; Prewitt, C. T. Revised Values of Effective Ionic Radii. *Acta Crystallogr. Sect. B Struct. Crystallogr. Cryst. Chem.* **1970**, *B26*, 1046–1048. https://doi.org/10.1107/s0567740870003576.

(32) Gani M.S.J. and McPherson R. Glass Formation and Phase Transformations in Plasma Prepared Al2O3-SiO2 Powders. *J. Mater. Sci.* **1977**, *12*, 999–1009.

(33) Gibbs, W. The Collected Works of J. Willard Gibbs. *Nature* **1929**, *124* (3117), 119–120. https://doi.org/10.1038/124119a0.

(34) Lacy, E. D. Aluminum in Glasses and Melts. *Phys. Chem. Glas.* **1963**, *4*, 234–238.

(35) Benmore, C. J.; Weber, J. K. R.; Wilding, M. C.; Du, J.; Parise, J. B. Temperature-Dependent Structural Heterogeneity in Calcium Silicate Liquids. *Phys. Rev. B - Condens. Matter Mater. Phys.* **2010**, *82* (22), 224202-1–6. https://doi.org/10.1103/PhysRevB.82.224202.

(36) Wilding, M. C.; Benmore, C. J.; Weber, J. K. R. Changes in the Local Environment Surrounding Magnesium Ions in Fragile MgO-SiO2 Liquids. *EPL (Europhysics Lett.* **2010**, *89* (2), 26005-p1–p5. https://doi.org/10.1209/0295-5075/89/26005.

(37) Urbain, G.; Bottinga, Y.; Richet, P. Viscosity of Liquid Silica, Silicates and Alumino-Silicates. *Geochim. Cosmochim. Acta* **1982**, *46* (6), 1061–1072. https://doi.org/10.1016/0016-7037(82)90059-X.

(38) Dingwell, D. B.; Courtial, P.; Giordano, D.; Nichols, A. R. L. Viscosity of Peridotite Liquid. *Earth Planet. Sci. Lett.* **2004**, *226* (1–2), 127–138. https://doi.org/10.1016/j.epsl.2004.07.017.

(39) Skinner, L. B.; Benmore, C. J.; Weber, J. K. R.; Wilding, M. C.; Tumber, S. K.; Parise, J. B. A Time Resolved High Energy X-Ray Diffraction Study of Cooling Liquid SiO2. *Phys. Chem. Chem. Phys.* **2013**, *15* (22), 8566–8572. https://doi.org/10.1039/c3cp44347g.

For TOC Only

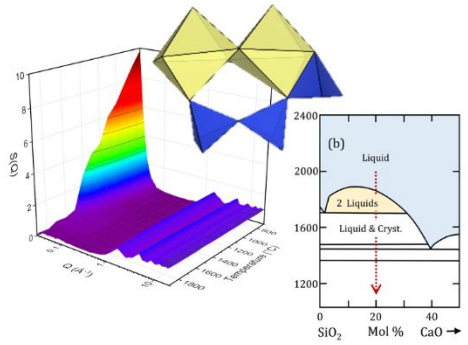
S(Q)
Q (Å⁻¹)
Temperature (C)
(b)
Liquid
2 Liquids
Liquid & Cryst.
2400
2000
1600
1200
0
20
40
SiO2
Mol %
CaO

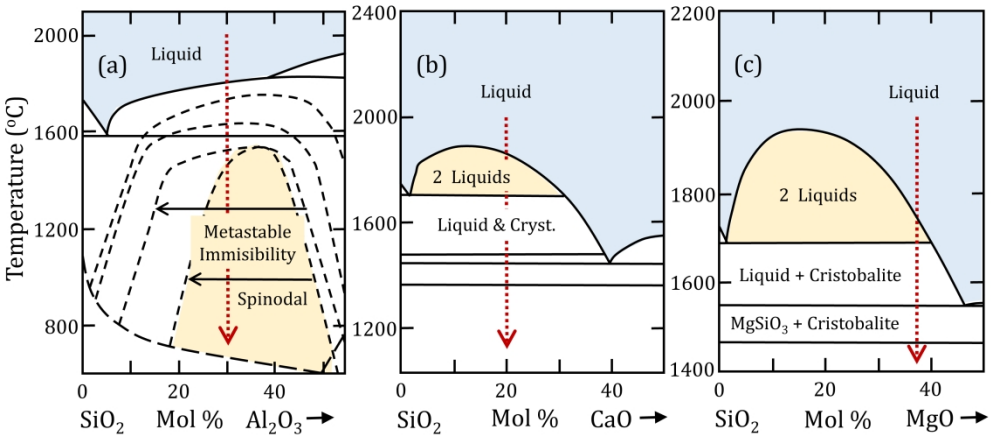

Figure1. Phase diagrams of (a) Al2O3-SiO2[4] (b) CaO-SiO2[8,9] and (c) MgO-SiO2[10,11]. The dashed black lines represent metastable phase boundaries and the red dotted lines represent the compositions studied here.

338x190mm (300 x 300 DPI)

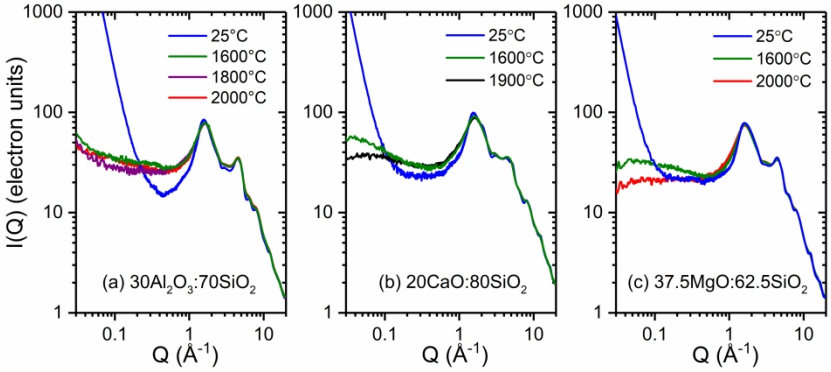

Figure 2. Normalized SAXS-WAXS intensities obtained from isothermal measurements on single phase liquid and two phase glassy silicates.

381x152mm (300 x 300 DPI)

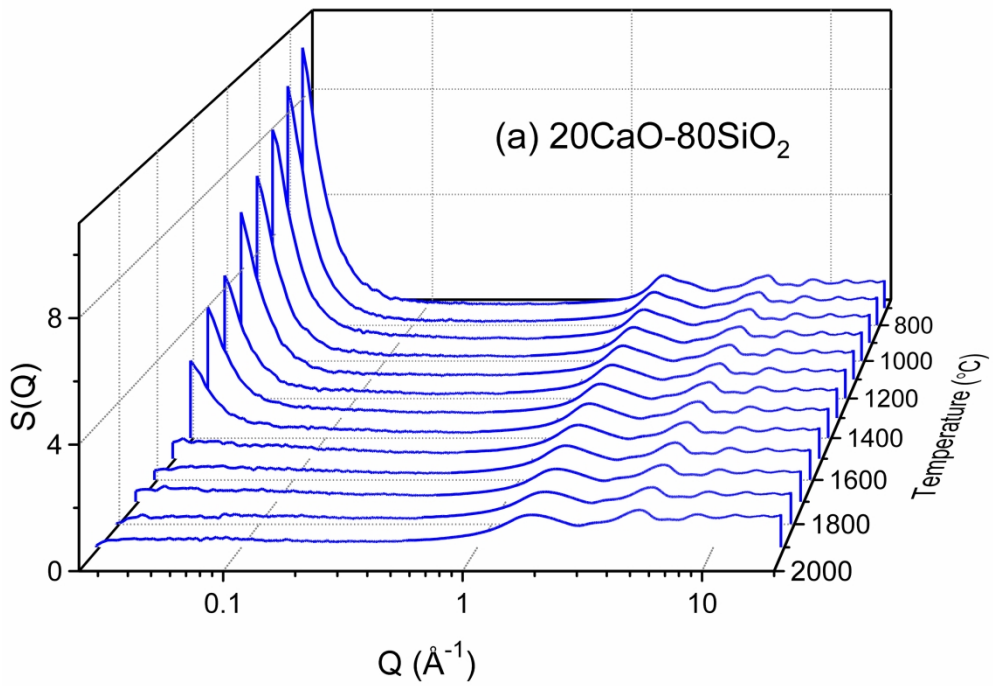

Figure 3(a). The SAXS-WAXS total x-ray structure factor changing from liquid to glass as a function of temperature during the quenching experiments for CS20.

272x203mm (300 x 300 DPI)

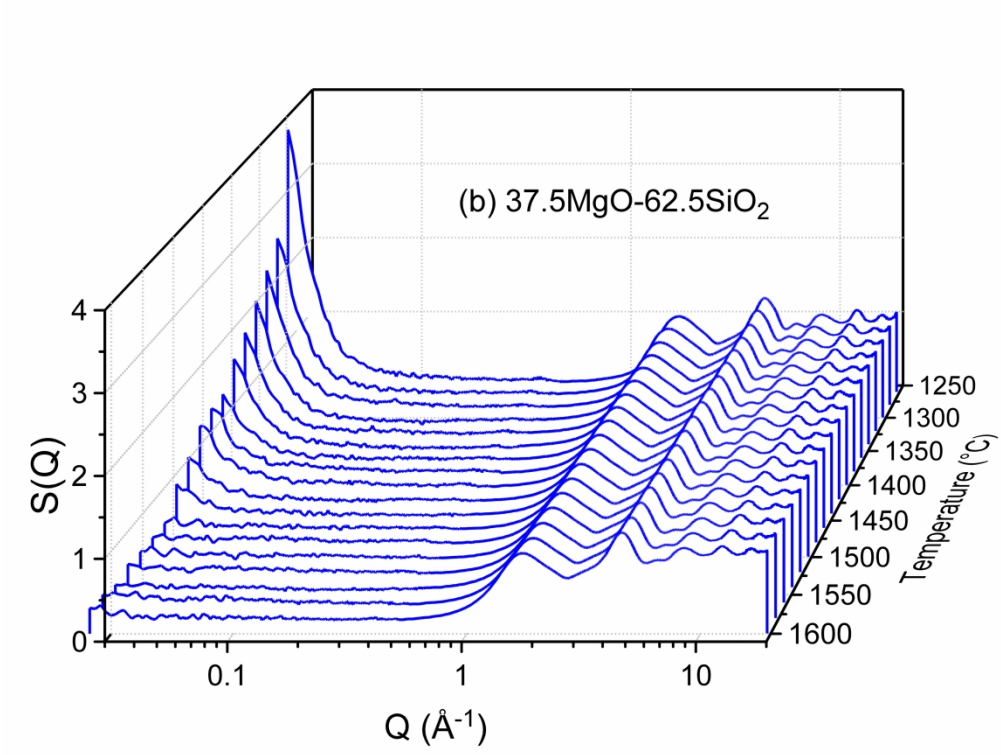

Figure 3(b). The SAXS-WAXS total x-ray structure factor changing from liquid to glass as a function of temperature during the quenching experiments for MS37.5.

272x208mm (300 x 300 DPI)

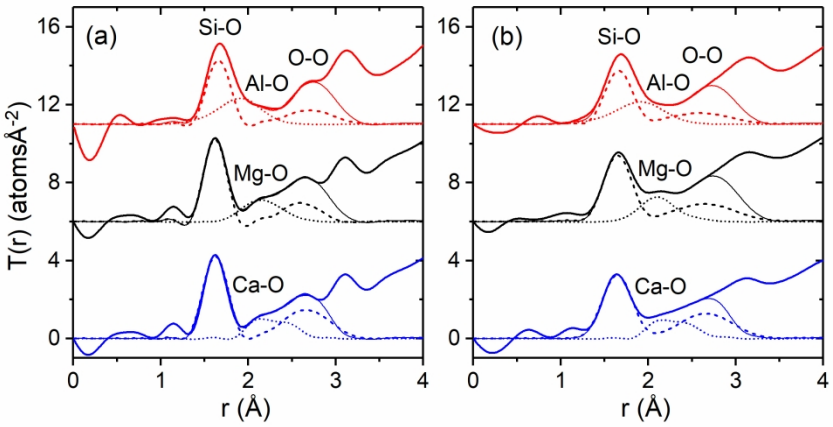

Figure 4. Total x-ray pair distribution functions for the isothermal experiments on binary silicates in the (a) room temperature glass and (b) liquid at 1600oC. The PDF data (thick solid lines) are shown as a function of increasing cation size: 30Al2O3:70SiO2 (top), 37.5MgO:62.5SiO2 (middle) and 20CaO:80SiO2 (bottom). The Gaussian fits described in the text correspond to the Si-O and O-O correlations associated with SiO4 tetrahedra (dashed line), the modifier cation-oxygen correlations (dotted line) and the total fit which includes short modifier O-O correlations (thin solid line).

254x127mm (300 x 300 DPI)

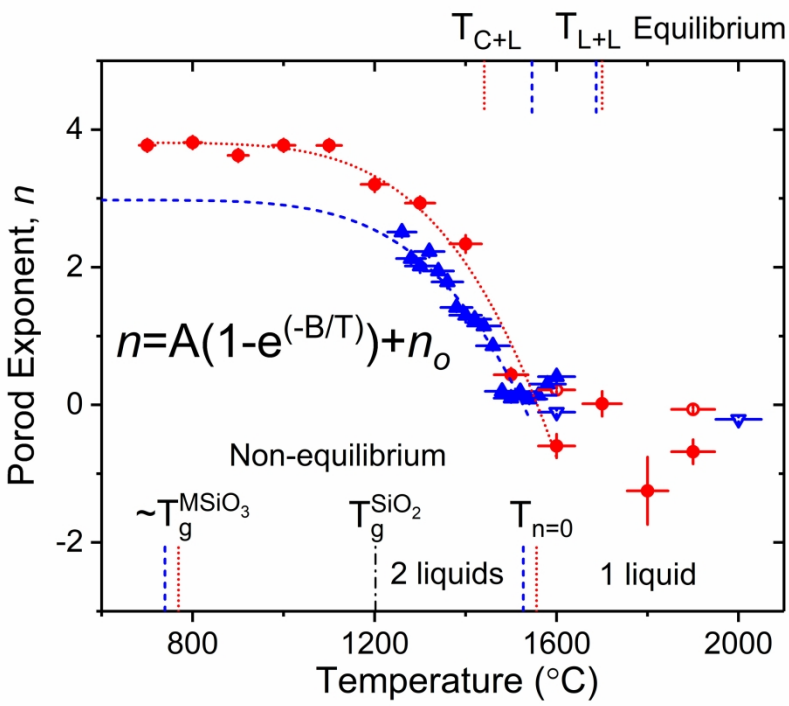

Figure 5. Temperature variation of the Porod exponent, n, in I(Q) for liquid 20CaO:80SiO2 (red circles denotes quenched sample experiments and red open circles the isothermal measurements) and liquid 37.5MgO:62.5SiO2 (blue solid up-triangles denotes quenched sample experiments and blue open-down triangles the isothermal measurements). The curves represent Arrhenius fits to the data. The markings at the top correspond to the equilibrium phase diagram temperatures: the lower 2-phase liquid boundary (TL+L) and the crystal plus liquid boundary below (TC+L). The markings at the bottom correspond to the non-equilibrium temperatures: the pure SiO2 glass transition temperature (TgSiO2), the single phase MSiO3 glass transition temperatures (TgMSiO3) and the temperatures at which the fits cross n=0 (Tn=0).

272x208mm (300 x 300 DPI)

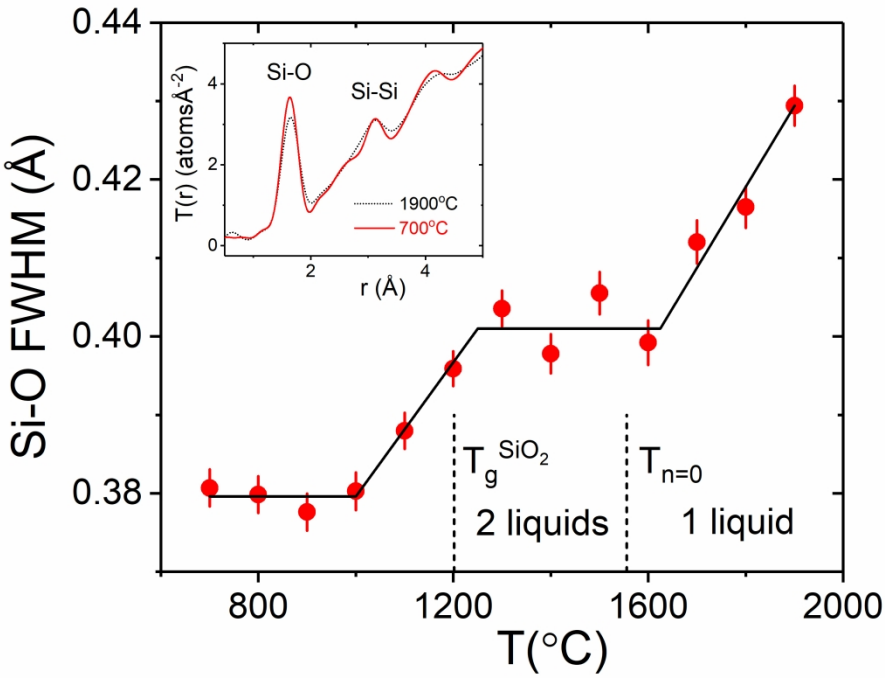

Figure 6. The change in full width half maximum of the Si-O peak upon cooling. Insert. The total pair distribution functions of 20CaO:80SiO2 liquid and glass. The SiO2 glass transition temperature (TgSiO2) and temperature at which phase separation begins in the SAXS signal (Tn=0) are marked. The line is a guide to the eye.

272x208mm (300 x 300 DPI)

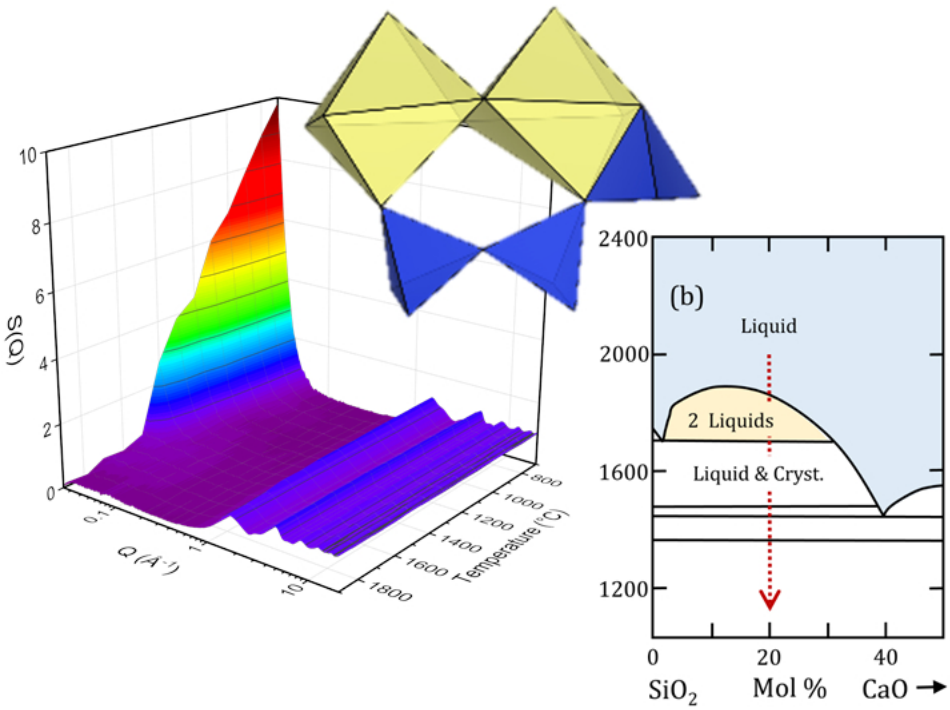

SAXS signal associated with liquid-liquid phase separation in silicate melts

63x45mm (300 x 300 DPI)